

A high-fidelity and large-scale reconfigurable photonic processor for NISQ applications

A. Cavallès,^{1,*} P. Boucher,² L. Daudet,¹ I. Carron,¹ S. Gigan,^{1,3} and K. Müller¹

¹*LightOn, 3-5 Impasse Reille, 75014 Paris, France.*

²*Quantum Metrology and Nano Technologies Division, INRiM, Strada delle Cacce 91, 10153 Torino, Italy.*

³*Laboratoire Kastler Brossel, ENS-Université PSL, CNRS, Sorbonne Université, Collège de France, 24 Rue Lhomond, F-75005, Paris, France.*

(Dated: May 12, 2022)

Reconfigurable linear optical networks are a key component for the development of optical quantum information processing platforms in the NISQ era and beyond. We report the implementation of such a device based on an innovative design that uses the mode mixing of a multimode fiber in combination with the programmable wavefront shaping of a SLM. The capabilities of the platform are explored in the classical regime. For up to a record number of 8 inputs and 38 outputs we achieve fidelities in excess of 93%, week-long stability and losses below 6.5dB. The device was built inside a standard server rack to allow for real world use.

I. LINEAR OPTICAL QUANTUM COMPUTING

Photons are excellent carriers of quantum information: They are resistant to decoherence and can easily propagate over large distances. Mature technologies for controlling their creation, propagation, and detection are now available, or on the cusp of becoming useful. They also allow to interface between other quantum platforms like ions [1], neutral atoms [2], spin [3] and superconducting qubits [4]. Taken together, these properties give them a unique standing in the development of applications in the NISQ era and beyond.

A recent implementation of optical quantum information processing (QIP [5]) demonstrated supremacy over classical computers for the first time, but only for one specific and fixed task [6]. One of the most promising avenues for practical and scalable optical QIP are programmable linear optical networks [7–9]. They are needed to implement QIP both in circuit model [10] and cluster state approaches [11, 12], and could find applications in diverse fields such as quantum transport [13–16], quantum repeaters [17], and quantum machine learning [18–21]. Photonic integrated circuits are a popular choice for the implementation of such systems [22–26]. Here the linear circuit is implemented via the propagation of light through a series of beam splitters and phase shifters in an integrated waveguide architecture. These systems see steady improvement, but their scalability is currently hindered by fabrication complexity, thermal stability and electrical control.

3D wave mixing in complex media in conjunction with wavefront shaping is a promising alternative approach. The implementation of a simple beam splitter [27–30] as well as more complex linear circuits [31, 32] have been demonstrated. Due to the much larger number of available propagation modes this type of system promises scalability beyond what can reasonably be achieved with

integrated circuits. Furthermore, there is the possibility to interface with a wider range of optical systems of various wavelengths including outside the NIR/telecom range. Demonstrations so far have been proofs of concepts in a laboratory environment. To enable their use in the ever-expanding context of NISQ, QIP necessitates more integrated and transportable designs. Furthermore, while this approach has been tested for circuits with up to 2 input ports, many applications require a larger circuit, in particular when working with dual-rail encoding [33].

In this paper, we report on the realization of a multimode-fiber-based optical linear processor installed in a standard server rack. After a classical characterization it is shown to allow for arbitrary linear quantum circuits with size up to 8×38 , fidelities above 93% and losses below 6.5 dB. We describe the so-called QORE processor and its working principle before providing a study of its performance in the classical regime in terms of circuit fidelity, stability and coupling.

II. QORE: PRINCIPLE

The operating principle of the device is shown in Fig. 1(a). The process harnesses the polarization and spatial mode-mixing properties of a multimode fiber (MMF) in conjunction with the wavefront shaping capabilities of a spatial light modulator (SLM) to implement the desired optical circuit \mathcal{L} . The wavefronts of incoming input fields on the left of the figure are shaped through the application of suitable phase masks on the SLM before being coupled into the MMF. The output fields are then verified to follow \mathcal{L} , both in the classical regime or using single photon detectors.

Each incoming input field is mapped onto the appropriate modes of the MMF in two steps. First the measurement of the MMF's transfer matrix (TM) is performed following a phase-stepping holographic method [34, 35]. The TM can then be inverted and applied to the target output coupling for the railing. In a final step, we fine-tune the parameters with an optimization algorithm to

* adrien@lighton.io

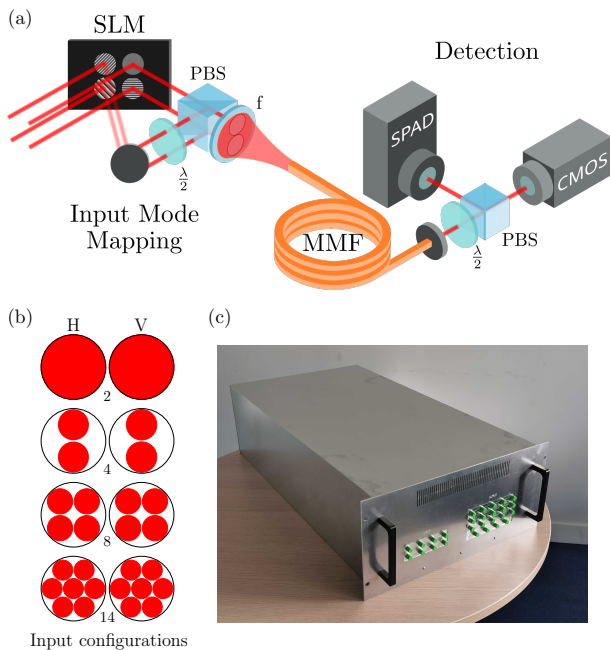


FIG. 1. **Device and principle.** (a): *Operating principle.* Incoming input modes are mapped controllably onto the spatial modes of a multimode fiber using a spatial light modulator (SLM). Orthogonal polarizations can be combined via a polarizing beam splitter (PBS) to double the number of inputs. A calibration phase where the output field is monitored while applying various phase masks on the SLM allows the computation of the MMF’s transfer matrix TM . Its inverse is then used to implement controlled circuits characterized both in the classical regime via either a CMOS camera or single-photon detector array (SPAD). (b): *Input scaling.* Increasing the number of inputs leads to lowering the number of accessible modes in the fiber. Black circle: fiber numerical aperture, red disks: input modes in different input configurations. By resizing and offsetting the input fields, it is possible to assess the scaling properties of the system. (c): *Prototype device.* Mechanical and thermal stability have been optimized for a rack-ready system.

achieve the best performance. Repeating the procedure for each input leads to the realization of a circuit \mathcal{L}_{exp} that can be compared with the targeted \mathcal{L} . The possibility of implementing a wide range of circuits is due to the largely isotropic polarization and spatial mode mixing taking place in the MMF, the many available degrees of freedom on the SLM as well as the unitary nature of the TM .

The concept has been presented and used in [31, 32] in the context of up to two optical inputs distinct in polarization. Here we report the extension of the system to 8 inputs as well as its characterization. Each input is incident on the SLM (Holoeye Pluto-2-NIR-080) as a gaussian beam before the appropriate phase masks are applied. The SLM is in the Fourier plane relative to the input facet of the MMF. Figure 1(b) shows the input beams in that plane in red. The MMF aperture (shown

as a black circle) limits the acceptable range of input modes. One can see that the available area for each input decreases as their number grows. Consequently the number of MMF modes per input decreases, leading to a change in performance that we characterize in section III. As an illustration, Fig. 1(a) shows the configuration corresponding to 2 input railings per polarization. We tested the system for configurations going up to 8 inputs.

Along with the input basis, the realization of optical circuits requires the definition of an output basis, or railings. Ultimately, these output railings aim to be matched to detection or propagation channels. In our case the quality of circuits is tested using two kinds of detection systems: a CMOS camera (Basler aca2000) and an array of 23 avalanche photodiodes (Pi Imaging SPAD23). Both are imaging the output facet of the MMF. The rotation of the half-waveplate at the output allows us to monitor both polarizations either with the camera or the single-photon detector array. With the camera, the output modes are defined as a set of zones on the sensor with an area on the order of the speckle grain size. In the case of the SPAD23, a total of 46 output modes are defined as the active areas of the 23 detectors, monitored on both polarizations. With these definitions set, one can see that we are able to evaluate the performance of the system in a variety of input-output number configurations $n \times m$ using a single input beam: To adapt to the input configuration n , we simply offset the beam on the SLM plane by the corresponding distance and then monitor m detection modes to match the output setting.

III. QORE: CAPABILITY

In Figures 2(a) and 2(b), we present experimentally implemented circuits as measured using the SPAD23 in the configuration corresponding to 2 inputs and variable output number settings. Fig 2(b) in particular illustrates the control we have on the circuit generation in the case of 38 outputs. As shown on top, we used here as a target circuit a non-unitary matrix reproducing the LightOn logo. Each line of the matrix was implemented in sequence and then measured to obtain the data-set displayed on the bottom. From this information, the quality of the implemented optical circuits can be assessed through two measures: circuit fidelity and transmission loss. The fidelity is an indication of how close the implemented circuit \mathcal{L}_{exp} is to the targeted one \mathcal{L}_{target} and is expressed as the trace of the product between the two: $\mathcal{F} = \frac{1}{D} \text{Tr}(\mathcal{L}_{exp} \mathcal{L}_{target}^\dagger)$, with D the dimension of \mathcal{L}_{exp} . The upper bound of \mathcal{F} is one. In practice we record the related statistical fidelity defined as $\mathcal{F} = \frac{1}{D} \text{Tr}(|\mathcal{L}_{exp}\rangle\langle\mathcal{L}_{target}|)$ in the output subspace, i.e. when correcting \mathcal{L}_{exp} for global transmission losses through its normalization. In the case of Fig. 2(b), for example we find an average statistical fidelity of 98.6%. The second measure is the transmission loss of a circuit, defined as the proportion of intensity at the input that is coupled into the targeted output

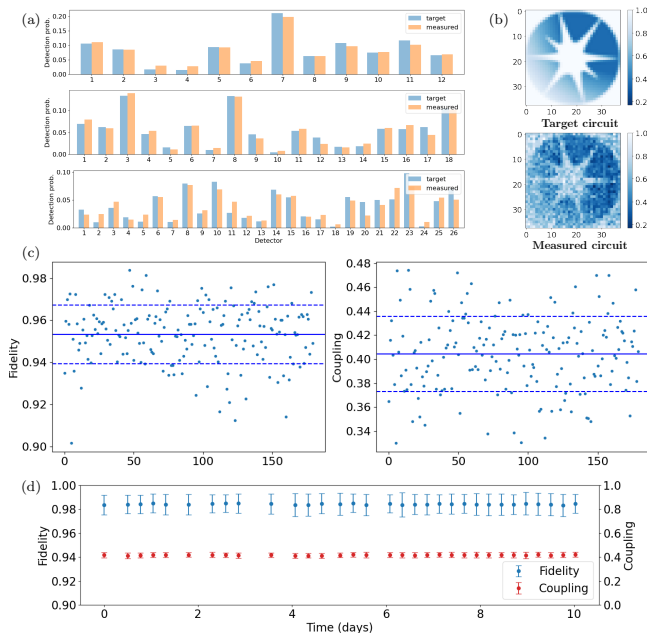


FIG. 2. **Performance of the device:** (a): Target vs measured detection probability for 3 example circuits using the SPAD23 detector array with 12, 18, and 28 outputs. (b): Example implementation of a 38x38 non-unitary target circuit. Each single input to 38 outputs amplitude distribution (corresponding to the lines of the matrix) has been measured separately in a 2-input configuration. The data-sets are re-normalized by their maxima. We measure a statistical fidelity of 98.6%. (c) Fidelity and coupling for 180 randomly distributed unitary circuits in 2x26 input-output configuration. Full line: mean, dashed lines: mean $\pm 1\sigma$. (d): Evolution of both parameters over 10 days without re-calibration. This characterization was done with the camera, in a 2x8 input-output configuration. Following a single-hour calibration the fidelity and coupling see no significant degradation over the period.

modes. The losses from the input up to the output of the fiber are directly measured using a Thorlabs PM100 power-meter. The SLM introduces losses through several properties. The 95% reflectivity of the screen directly translates into 5% of losses independently of the circuit. However, the losses resulting from its limited fill factor (93%) and diffraction efficiency will change with the displayed phase mask. The power-meter is therefore used to monitor the transmission through the fiber on a circuit-by-circuit basis. The remaining coupling into the output railings is assessed through an initial calibration procedure relating the power-meter and SPAD23 system detection efficiencies. In practice, this calibration is estimated to be accurate up to 6% of standard deviation. The last source of loss is due to reflections at every interface and is measured to be 10%. Since the application of anti-reflection coatings would greatly reduce this loss, we provide in table I values both with and without correction from reflection losses.

Following this methodology, we implemented ~ 100 unitary circuits \mathcal{L}_k , randomly chosen from the Haar measure, per input-output setting. For each circuit the fidelity and transmission loss was measured. The light source used is a superluminescent diode centered on 810 nm, and filtered by a 2 nm FWHM spectral filter. As we use a single input for the characterisation and unitary circuits are square, we implemented in sequence each line of \mathcal{L}_k and then averaged the values to obtain the overall circuit fidelity and loss. These two measures are shown in figure 2(c), in the case of 2 inputs and 26 outputs when measured using the SPAD23. We find an average fidelity of $95.3\% \pm 1\%$ and total coupling from input to detection mode averaging at 40% (which corresponds to 4 dB losses), and 45% when correcting for the reflection losses. The process has been repeated for a number of configurations and results are summarized in Table I. We obtain high values of statistical fidelities averaging above 93% for all considered input-output configurations and observe low variation in quality depending on the circuit at a fixed input size. This compares favorably with many alternative methods based on integrated circuits [23, 25] at comparable output sizes and is close to recent demonstrations [26] for 26 outputs. The ease of scaling to a larger number of outputs is one significant advantage of the 3D wave-mixing approach, as leading re-configurable integrated systems are currently limited to our knowledge to 20x20 circuits.

While the measured transmission loss is still high for specific usages such as quantum advantage demonstrations (~ 2 dB in [6]), it can be mitigated through various avenues. First, through the addition of anti-reflection coatings on the fiber; second, the independent control of two polarization channels at the input — instead of one in the current system — would lead to a decrease of losses. Another possibility would be the addition of input beam shaping to improve the packing at the SLM level, so that the number of spatial modes used by each input railing is greater. One should note as well that these results are intrinsically linked to the specific properties of the detector. We used a commercial system that is therefore not specifically designed for the procedure. In particular, increasing the fill-factor of the detection device beyond the SPAD23's 23.5% would lead to an improvement in circuit quality. The quality of implementation of the circuit will also depend on the temporal modes of the quantum states used. As all measurements have been performed at 810 ± 2 nm, it is therefore a worst-case scenario for narrower quantum sources. On the other hand, if a degradation in quality can be expected for broader sources, we note however that it can be mitigated through the adaptation of the multimode fiber properties, in particular its length. As it only monitors the circuits from a single input, our characterization method cannot take into account the background noise introduced by eventual other inputs coupled into the system. This effect could however be mitigated through an additional fine-tuning once all input masks have been obtained separately.

		2 inputs	4 inputs	8 inputs
Fidelity	14 outputs	97.1% \pm 1%	96.6% \pm 1%	96.3% \pm 1%
	26 outputs	95.3% \pm 1%	94.7% \pm 1%	94.2% \pm 1%
	38 outputs	93.7% \pm 1%	93.5% \pm 1%	92.9% \pm 1%
Losses	14-38 outputs	4.0(3.5*)dB \pm 0.5dB	5.1(4.6*)dB \pm 1dB	6.2(5.7*)dB \pm 1.2dB

TABLE I. Measured statistical fidelity and losses for different input-output configurations as measured on the SPAD23. *: Values estimated with the addition of anti-reflection coatings.

Another important aspect of the system is its stability over time. In Fig. 2(d) we plotted the measured fidelity and coupling for a fixed set of 160 2x8 circuits over more than 10 days after a single initial calibration. As one can see, there are variations in quality but no significant degradation over the whole period. These measurements were obtained with the rack set on an optical table with no active vibration system, laminar flow or temperature control in place. This level of stability can be therefore expected or exceeded in most settings where quantum sources or detection systems are used. The characterization of the transfer matrix takes about two hours per input mode to perform, meaning that the day-to-day use remains practical even for 8 inputs and beyond.

Two additional properties of the approach distinguish it from integrated alternatives. First, it is largely wavelength agnostic as the system can work over a wide range of wavelengths without specific adaptations, apart from the change of (anti-)reflection coatings and SLM model. Second, the circuit reconfiguration speed is fixed by the refresh rate of the modulator no matter the circuit size. While integrated systems of comparable dimensions typically require reconfiguration time in the order of 1s, the rate is in our case close to 10 Hz. In addition, ongoing developments of the SLM technology hold the promise of significantly faster updating. Commercial models exhibiting 700 Hz of refresh rate are already available while new architectures going to the MHz level

have been proposed [36]. These adaptations would significantly broaden the capabilities of the platform, allowing for example the consecutive application of gates conditioned on the results of preceding ones.

IV. CONCLUSION

In this paper, we have introduced and characterized a compact and linear optical processor based on complex mixing and wavefront shaping. We find that the platform brings significant benefits: advantageous scaling — as exemplified by the realisation of a record 38-output circuit —, high fidelities and competitive reconfiguration rate, while maintaining week-long stability. It represents as such a novel tool for optical QIP that could be used as a convincing alternative or in conjunction with integrated systems. The asymmetry of the implemented circuits suggests one exciting prospect in particular: the generation of high-dimensional entanglement from few single photon states, thus allowing the interconnection between many quantum platforms.

V. ACKNOWLEDGMENTS

We acknowledge support from EU Horizon 2020 FET-OPEN OPTOLogic (Grant No. 899794).

-
- [1] C. Monroe, R. Raussendorf, A. Ruthven, K. R. Brown, P. Maunz, L.-M. Duan, and J. Kim, *Phys. Rev. A* **89**, 022317 (2014).
 - [2] V. A. Pivovarov, A. S. Sheremet, L. V. Gerasimov, J. Laurat, and D. V. Kupriyanov, *Phys. Rev. A* **101**, 053858 (2020).
 - [3] K. C. Chen, E. Bersin, and D. Englund, *npj Quantum Inf* **7**, 1 (2021).
 - [4] S. Das, V. E. Elfving, S. Faez, and A. S. Sørensen, *Phys. Rev. Lett.* **118**, 140501 (2017).
 - [5] J. L. O'Brien, *Science* **318**, 1567 (2007).
 - [6] H.-S. Zhong, H. Wang, Y.-H. Deng, M.-C. Chen, L.-C. Peng, Y.-H. Luo, J. Qin, D. Wu, X. Ding, Y. Hu, P. Hu, X.-Y. Yang, W.-J. Zhang, H. Li, Y. Li, X. Jiang, L. Gan, G. Yang, L. You, Z. Wang, L. Li, N.-L. Liu, C.-Y. Lu, and J.-W. Pan, *Science* **370**, 1460 (2020).
 - [7] P. Kok, W. J. Munro, K. Nemoto, T. C. Ralph, J. P. Dowling, and G. J. Milburn, *Rev. Mod. Phys.* **79**, 135 (2007).
 - [8] N. C. Harris, J. Carolan, D. Bunandar, M. Prabhu, M. Hochberg, T. Baehr-Jones, M. L. Fanto, A. M. Smith, C. C. Tison, P. M. Alsing, and D. Englund, *Optica*, **5** 1623 (2018).
 - [9] T. R. Bromley, J. M. Arrazola, S. Jahangiri, J. Izaac, N. Quesada, A. D. Gran, M. Schuld, J. Swinerton, Z. Zabaneh, and N. Killoran, *Quantum Sci. Technol.* **5**, 034010 (2020).
 - [10] E. Knill, R. Laflamme, and G. J. Milburn, *Nature* **409**, 46 (2001).

- [11] R. Raussendorf and H. J. Briegel, *Phys. Rev. Lett.* **86**, 5188 (2001).
- [12] R. Raussendorf, D. E. Browne, and H. J. Briegel, *Phys. Rev. A* **68**, 022312 (2003).
- [13] A. Peruzzo, M. Lobino, J. C. F. Matthews, N. Matsuda, A. Politi, K. Poulios, X.-Q. Zhou, Y. Lahini, N. Ismail, K. Wörhoff, Y. Bromberg, Y. Silberberg, M. G. Thompson, and J. L. O'Brien, *Science* **329**, 1500 (2010).
- [14] A. Crespi, R. Osellame, R. Ramponi, V. Giovannetti, R. Fazio, L. Sansoni, F. De Nicola, F. Sciarrino, and P. Mataloni, *Nat. Photonics* **7**, 322 (2013).
- [15] C. Sparrow, E. Martín-López, N. Maraviglia, A. Neville, C. Harrold, J. Carolan, Y. N. Joglekar, T. Hashimoto, N. Matsuda, J. L. O'Brien, D. P. Tew, and A. Laing, *Nature* **557**, 660 (2018).
- [16] X. Qiang, Y. Wang, S. Xue, R. Ge, L. Chen, Y. Liu, A. Huang, X. Fu, P. Xu, T. Yi, F. Xu, M. Deng, J. B. Wang, J. D. A. Meinecke, J. C. F. Matthews, X. Cai, X. Yang, and J. Wu, *Science Advances* **7**, eabb8375 (2021).
- [17] Y. Lee, E. Bersin, A. Dahlberg, S. Wehner, and D. Englund, *arXiv:2005.01852* (2020).
- [18] Y. Shen, N. C. Harris, S. Skirlo, M. Prabhu, T. Baehr-Jones, M. Hochberg, X. Sun, S. Zhao, H. Larochelle, D. Englund, and M. Soljačić, *Nat. Photonics* **11**, 441 (2017).
- [19] G. R. Steinbrecher, J. P. Olson, D. Englund, and J. Carolan, *npj Quantum Inf* **5**, 1 (2019).
- [20] J. Feldmann, N. Youngblood, M. Karpov, H. Gehring, X. Li, M. Stappers, M. Le Gallo, X. Fu, A. Lukashchuk, A. S. Raja, J. Liu, C. D. Wright, A. Sebastian, T. J. Kippenberg, W. H. P. Pernice, and H. Bhaskaran, *Nature* **589**, 52 (2021).
- [21] V. Saggio, B. E. Asenbeck, A. Hamann, T. Strömberg, P. Schiansky, V. Dunjko, N. Friis, N. C. Harris, M. Hochberg, D. Englund, S. Wölk, H. J. Briegel, and P. Walther, *Nature* **591**, 229 (2021).
- [22] J. C. F. Matthews, A. Politi, A. Stefanov, and J. L. O'Brien, *Nat. Photonics* **3**, 346 (2009).
- [23] J. Carolan, C. Harrold, C. Sparrow, E. Martín-López, N. J. Russell, J. W. Silverstone, P. J. Shadbolt, N. Matsuda, M. Oguma, M. Itoh, G. D. Marshall, M. G. Thompson, J. C. F. Matthews, T. Hashimoto, J. L. O'Brien, and A. Laing, *Science* **349**, 711 (2015).
- [24] F. Flamini, N. Spagnolo, and F. Sciarrino, *Rep. Prog. Phys.* **82**, 016001 (2018).
- [25] C. Taballione, R. van der Meer, H. J. Sniijders, P. Hooijschuur, J. P. Epping, M. de Goede, B. Kassenberg, P. Venderbosch, C. Toebes, H. van den Vlekkert, P. W. H. Pinkse, and J. J. Renema, *Mater. Quantum. Technol.* (2021).
- [26] C. Taballione, M. C. Anguita, M. de Goede, P. Venderbosch, B. Kassenberg, H. Sniijders, N. Kannan, D. Smith, J. P. Epping, R. van der Meer, P. W. H. Pinkse, H. van den Vlekkert, and J. J. Renema, *arXiv:2203.01801* (2022).
- [27] S. R. Huisman, T. J. Huisman, S. A. Goorden, A. P. Mosk, and P. W. H. Pinkse, *Opt. Express*, **22**, 8320 (2014).
- [28] S. R. Huisman, T. J. Huisman, T. A. W. Wolterink, A. P. Mosk, and P. W. H. Pinkse, *Opt. Express*, **23**, 3102 (2015).
- [29] T. A. W. Wolterink, R. Uppu, G. Ctistis, W. L. Vos, K.-J. Boller, and P. W. H. Pinkse, *Phys. Rev. A* **93**, 053817 (2016).
- [30] H. Defienne, M. Barbieri, I. A. Walmsley, B. J. Smith, and S. Gigan, *Science Advances* **2**, e1501054 (2016).
- [31] S. Leedumrongwatthanakun, L. Innocenti, H. Defienne, T. Juffmann, A. Ferraro, M. Paternostro, and S. Gigan, *Nat. Photonics* **14**, 139 (2020).
- [32] S. Goel, S. Leedumrongwatthanakun, N. H. Valencia, W. McCutcheon, C. Conti, P. W. H. Pinkse, and M. Malik, *arXiv:2204.00578* (2022).
- [33] S. Bartolucci, P. M. Birchall, M. Gimeno-Segovia, E. Johnston, K. Kieling, M. Pant, T. Rudolph, J. Smith, C. Sparrow, and M. D. Vidrighin, *arXiv:2106.13825* (2021).
- [34] S. M. Popoff, G. Lerosey, R. Carminati, M. Fink, A. C. Boccara, and S. Gigan, *Phys. Rev. Lett.* **104**, 100601 (2010).
- [35] T. Čížmár, and K. Dholakia, *Opt. Express*, **19**, 18871 (2011).
- [36] C. Peng, R. Hamerly, M. Soltani, and D. R. Englund, *Opt. Express*, **27**, 30669 (2019).